Schweizerischer Erdbebendienst
Service Sismologique Suisse
Servizio Sismico Svizzero
Swiss Seismological Service

ETH zürich

SITE CHARACTERIZATION REPORT
SNES2: Neuchâtel (NE), Observatoire

Paolo Bergamo, Manuel Hobiger, Stefano Maranò, Donat Fäh

Last modificaction: 01.02.2019

Schweizerischer Erdbebendienst (SED)
Service Sismologique Suisse
Servizio Sismologico Svizzero
Servizi da Terratrembels Svizzer

ETH Zurich
Sonnegstrasse 5
8092 Zuerich
Schweiz
paolo.bergamo@sed.ethz.ch

Contents

Summary

The new SSMNet station SNES2 was installed on 5 December 2014 close to the Cantonal Observatory of Neuchâtel, itself located north-east of the city center, at the top of a low, elongated ridge extending from south-west to north-east. Active and passive seismic measurements were performed to characterize the subsurface structure beneath the station. The results indicate that station SNES2 is hosted in a stiff site (V_{S30} = 1021 m/s), as the seismic bedrock is shallow (encountered at an estimated depth of approximately 10 m) and characterized by a high value of shear-wave velocity of around 1600 m/s. The identified soil class is therefore class A according to both Eurocode 8 (CEN, 2004) and SIA261 (SIA, 2014) regulations. The bedrock is probably constituted by limestone, locally topped by a layer of stiff soil (probably moraine, with V_S around 600 m/s). The fundamental frequency of the site is around 2 Hz, and it is likely to be ascribed to a rock-to-rock interface at a depth beyond the penetration capability of the performed surveys. At higher frequencies, approximately 13 Hz, another peak can be identified in both H/V curves and in the empirical amplification function from spectral modeling of SNES2; this feature can be attributed to the resonance frequency of the ridge.

1. Introduction.

In the framework of the second phase of the SSMNet (Swiss Strong Motion Network) renewal project, a new station, labelled as SNES2, was installed on 5 December 2014 in vicinity of the Cantonal Observatory, in the municipality of Neuchâtel (Figure 1). The Observatory and station SNES2 are located on the top of a low (difference in elevation with respect to surrounding areas of about 10 m), elongated ridge (about 370 m long and 40 m wide), stretching from south-west to north-east, itself situated north-east of the city center of Neuchâtel. Active and passive seismic surveys were carried out at this location to characterize the subsurface beneath station SNES2.

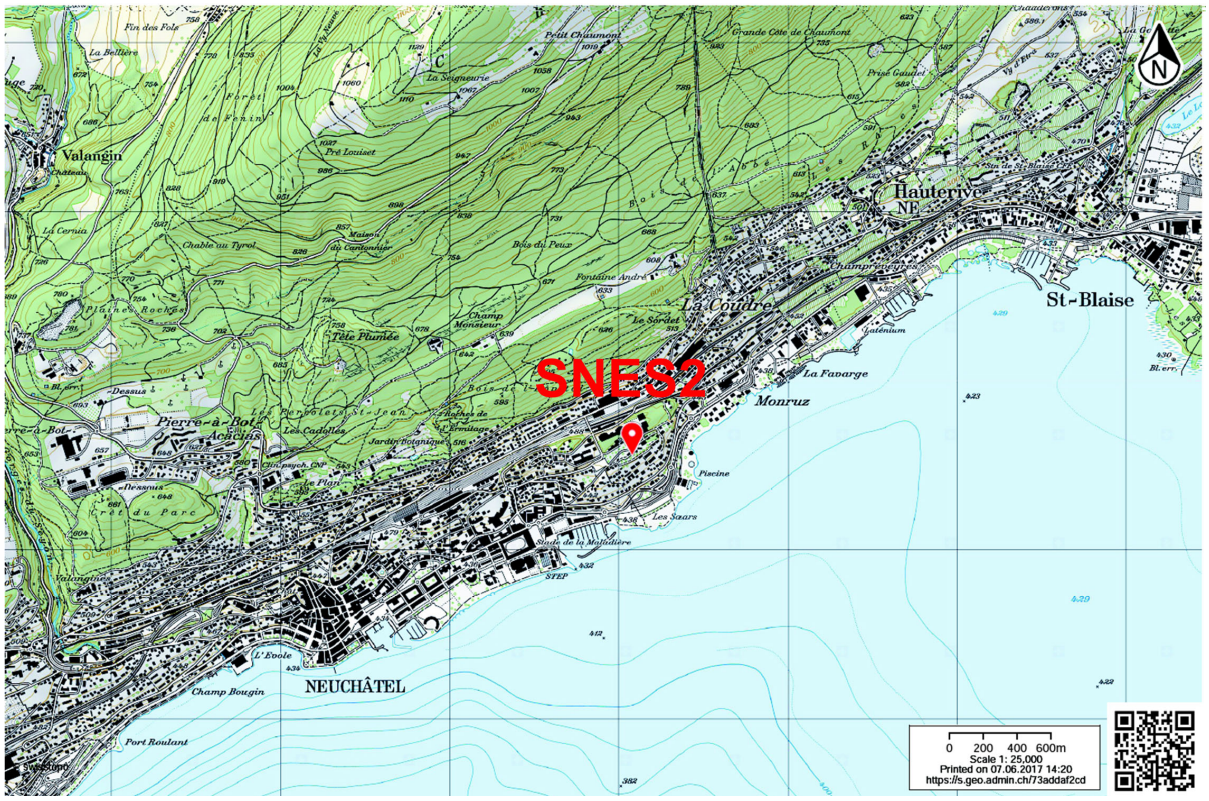

Figure 1 – Position of station SNES2 with respect to the urban area of Neuchâtel.
©2019 swisstopo (JD100042)

2. Site presentation

The site of the Observatory in Neuchâtel is one of the most important ones for the history of seismology in Switzerland. Between 1922 and 1934, four seismic stations of the Quervain-Piccard type were installed in Switzerland. These universal seismographs consisted of a moving mass of 21 t and were capable to record the three-component motion of the underground on soot paper.
One of these four seismographs (station code NEU) was installed in the Observatory building in Neuchâtel (Figure 2) in 1926. The sensor is still in place today and is therefore the last remaining of these four instruments. The other three instruments were installed in Binningen close to Basel (BAS), Zurich (ZUR) and Chur (CHU).
The recordings of station NEU were used until the 1970s, although the instrument could in principle still be operational today. In November 1989, one of the first strong-motion stations in Switzerland, SNES, was installed next to the old seismograph (Figure 3). This station was recording in triggered mode, i.e. only when the acceleration exceeded a certain threshold. This station was operational until 2005, but it recorded only six earthquakes during its living time. The recorder is still installed next to the old seismograph.
Taking the long history of seismic recordings in Neuchâtel into account, it was decided to renew station SNES with a modern strong-motion sensor. In order to avoid the disturbances of the building on the recordings, it was decided to build the station outside and to place it inside the MeteoSwiss weather station (Figure 4). The new station, SNES2, is located in a distance of about 17 m from the previous stations NEU and SNES.
The almost hundred years of seismic instrumentation, together with the three instruments that were installed and are still in place today, make the Observatory of Neuchâtel a special site for the history of seismology in Switzerland.

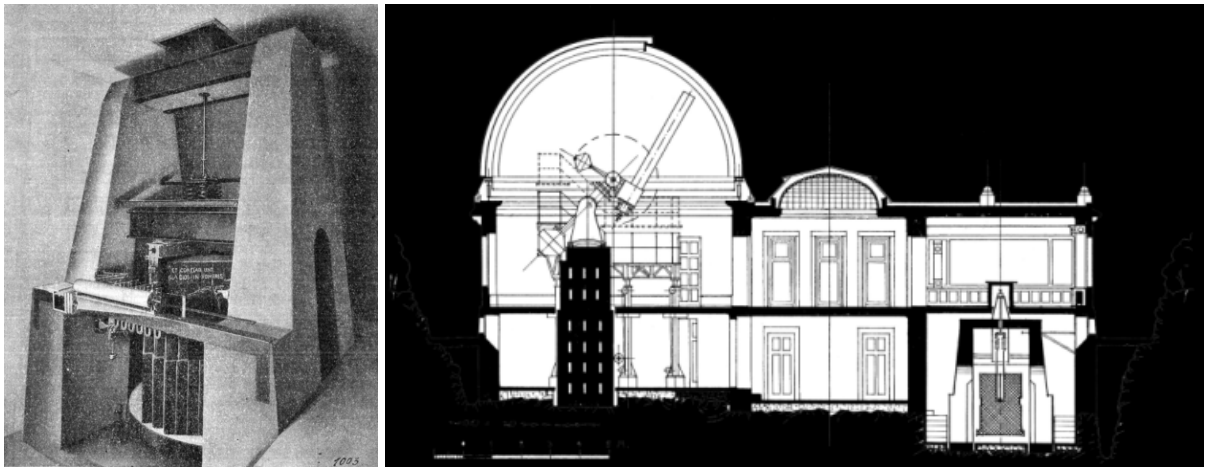

Figure 2 – Photograph of station NEU (left) and its location inside the Observatory building (right). The station is installed below the meeting room on the right.

Figure 3 – Photographs of the strong-motion station SNES. The sensor (left) is placed on the ground next to NEU. The datalogger (right) is located on the wall and the data can be accessed by a modem connection.

Figure 4 – The new station SNES2 is located inside the MeteoSwiss weather station, in the big vault to the right.

3. Geological setting

The geological cover of the area of the municipality of Neuchâtel is mainly constituted by belts of outcropping limestone, stretching from north-east to south-west, intertwined with strips of moraine, alluvial deposits, or artificial fill (Figure 5, top). Below the surface, we find a succession of limestone layers parallel to the shore of the lake of Neuchâtel and inclined towards north-west (Figure 5, bottom). The Observatory and station SNES2 are located on top of one of these limestone outcrops.

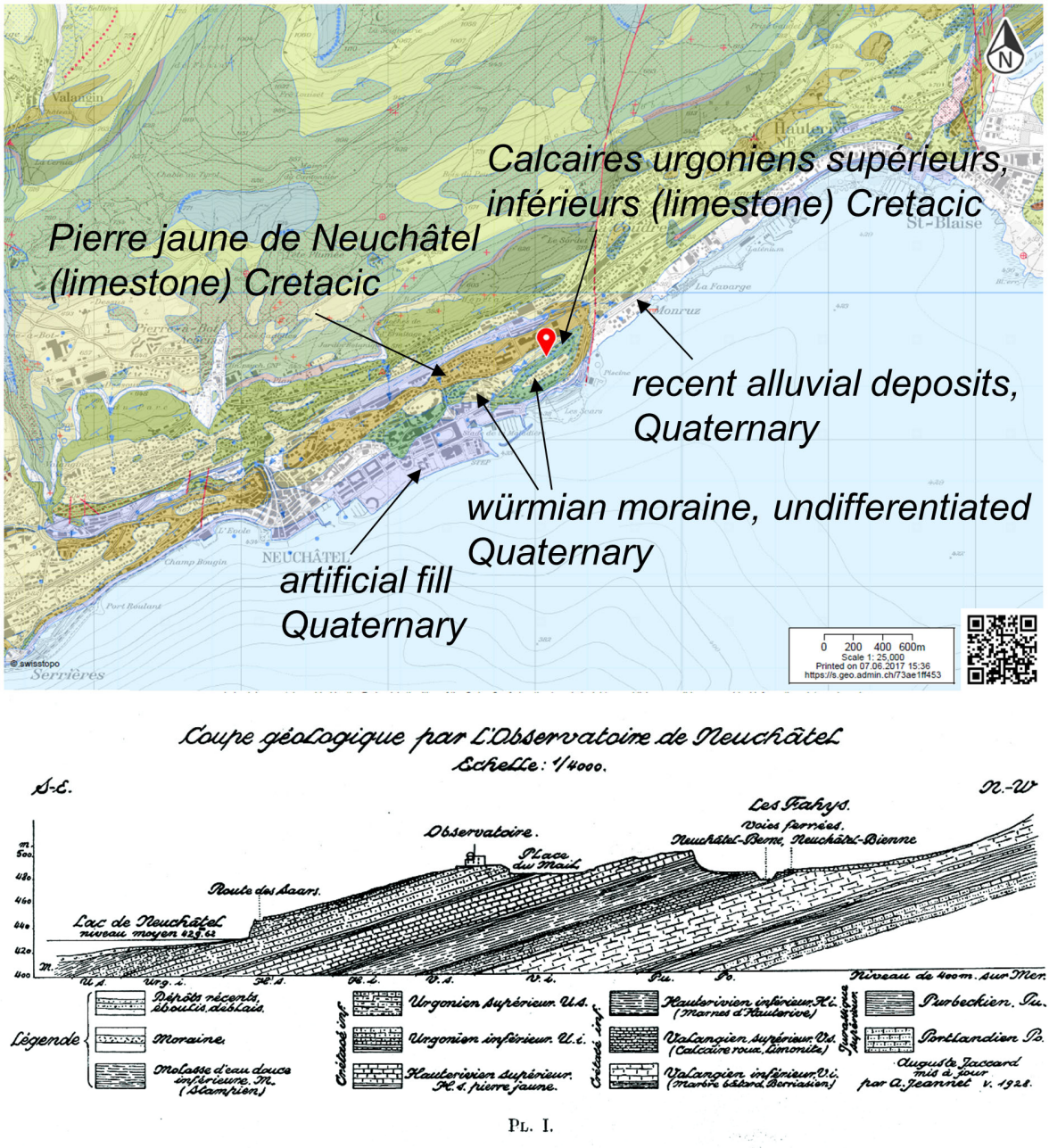

Figure 5 – top: location of station SNES2 on the map of Swiss geological atlases 1:25000. © 2019 Swisstopo, JD100042. Bottom: geological section along a south-east/north-west axis of the area of the Cantonal Observatory (Arndt, 1932).

4. Seismic acquisition

Active and passive seismic measurements were performed around SNES2 on 6 March 2015. The passive seismic array, consisting of 20 seismic sensors, was installed first and recording as undisturbed as possible for 80 minutes. Afterwards, a line of 24 geophones was deployed along the road close to station SNES2. Active seismic measurements were performed using a sledgehammer as seismic source at nine different shot points. The passive array was also recording these active signals, in order to test the WaveDecActive code (Maranò et al., 2017). The locations of the passive sensors, the geophones and the shot points with respect to station SNES2 are shown in Fig. 6.

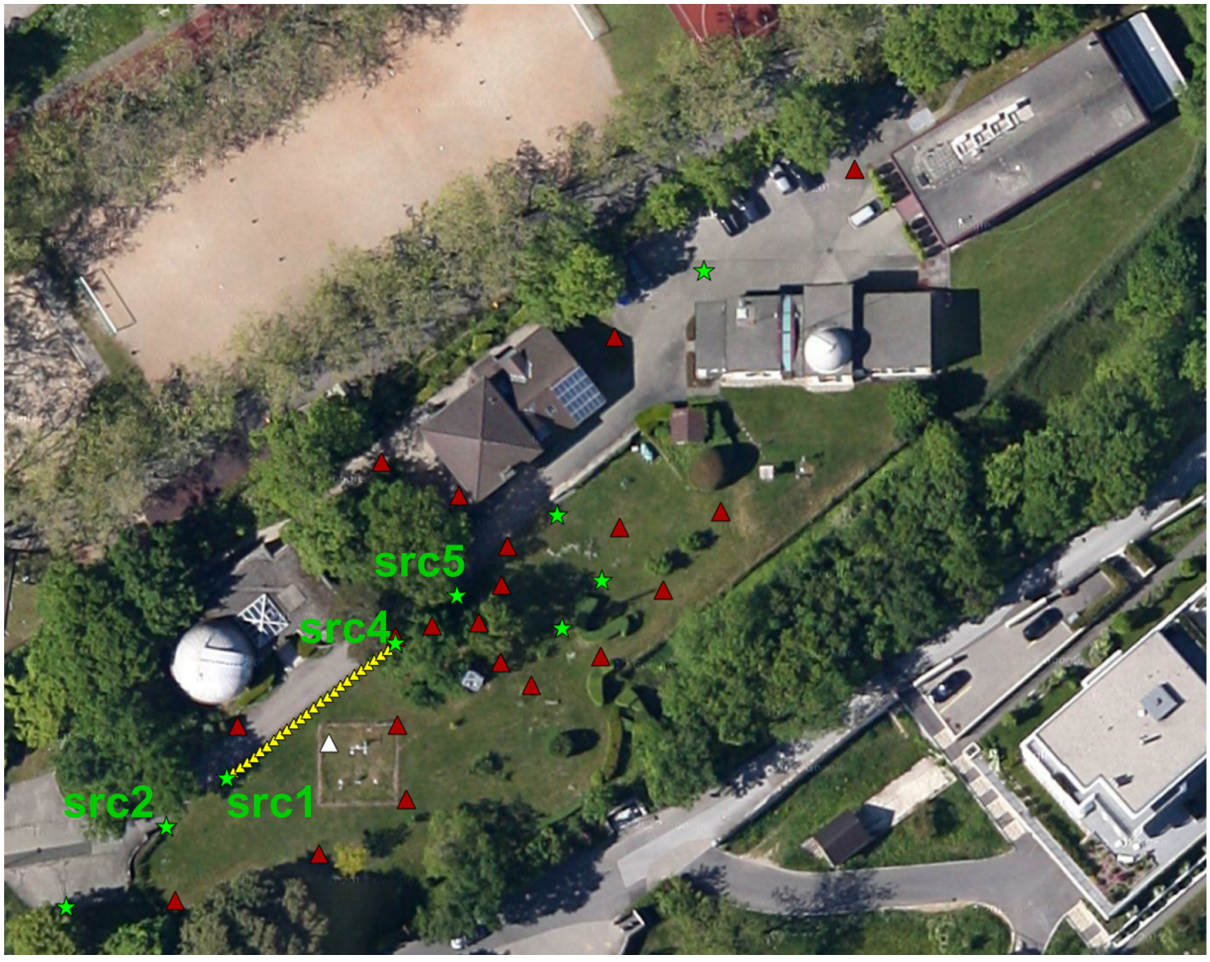

Figure 6 – Acquisition arrays. Sensors for microtremor recording (passive array) are indicated with red triangles; the geophones from the active line are indicated with yellow triangles. The hammering positions are indicated by the green stars; those used for the processing of MASW data are labeled src1,2,4,5. Station SNES2 is represented as a white triangle. © 2019 swisstopo (JD100042)

4.1 Passive seismic acquisition

The elongated ridge, on which the station is located, made the array design difficult. The array optimization code of Maranò et al. (2014) was used to optimize the central part of the array, consisting of 13 stations, which were located along three 'spiral' arms around a central station. The innermost stations had a distance of about 5.2 m from the central station, the stations on the next ring of about 9.5 m, followed by about 15 m and 21.9 m, respectively. Seven further stations were deployed to fill up the ridge more or less evenly. The minimum and maximum inter-station distances of the array were 4.4 m and 115.4 m, respectively. The recording time of the passive array was 80 minutes.
Each station consisted of a Lennartz 5s sensor connected to a Quanterra Q330 digitizer. In total, the 20 sensors were connected to 12 digitizers, so that eight digitizers were connected to two sensors.
The station locations have been measured by a differential GPS system (Leica Viva GS10) which was set up to measure with a precision better than 5 cm. This precision was obtained for 16 stations, four stations had rather high precision errors of 0.09 m, 0.15 m, 0.29 m and 0.59 m, respectively. The stations with the high precision errors were located underneath trees in the center of the array.

4.2 Active survey

To ensure investigation coverage also at higher frequencies, and to investigate in detail the shallow near-surface at the location of station SNES2, an active survey was conducted after the passive recording. For the sake of a comprehensive subsurface characterization, multichannel analysis of surface waves (MASW; Park et al., 1999) and P-wave refraction (Redpath, 1973) acquisitions were conducted.

4.2.1 Equipment and geometry of the acquisition array

The seismic source was a 5-kg sledgehammer, successively positioned at 9 different locations (green stars in Figure 6). For the acquisition of active seismic traces, we used both the Lennartz sensors from the passive array, and a line of geophones deployed in close proximity to station SNES2 (Figures 6 and 7). The line was constituted by three sets of eight three-component geophones (4.5 Hz corner frequency), for a total of 24 receivers positioned at regular intervals of 1 m. Each geophone set was connected to a Geode datalogger; the three Geodes were coupled for time synchronization. The locations of the geophones and seismic sources were also measured using the differential GPS.
All 9 shooting positions were used to generate seismic traces to be acquired by the Lennartz sensors from the passive array, to be later processed for Rayleigh wave analysis; 4 of these 9 positions, in-line with the geophone array and at 1 and 10 m from the outer receivers, were exploited to generate seismic traces to be recorded by the geophone spread, and later processed for Love and Rayleigh wave analysis and also P-wave refraction analysis. At all 9 shooting position, the hammer was repeatedly (10 times in most cases) released vertically on a flat metal plate, for P-SV wave excitation; at two positions, src2 and src5, besides the flat plate, also a wedge-shaped metallic frame was used for SH wave excitation. The plate is an isosceles right triangle: the hypotenuse is placed on the ground, and coupled to it with spikes penetrating the soil. The catheti are oriented orthogonally to the geophone spread, and alternately hit with the hammer; here again, 10 blows were exerted on each side of the wedge.

The synchronization between the traces recorded by the geophones and the seismic source was ensured by a trigger device fastened to the hammer handle.

Figure 7 – Deployed geophone spread. Beyond the fence on the left is the vault covering station SNES2.

4.2.2 Acquisition

For the geophone line acquisition, the time-sampling parameters adopted for both MASW and refraction acquisitions were the following: sampling interval = 0.125 ms, record length = 1 s, pre-trigger delay = 0 s. Figure 8 shows two sample seismic sections, one (left) representing the vertical component traces obtained by hitting the flat plate with a vertical blow of the hammer (pure P-SV excitation), the other representing the transversal component traces obtained by hitting the wedge plate on one of its sides. In both insets, the wave train generated by the hammer blows is clearly visible; it appears to fade at 0.15 s already, suggesting high velocities of propagation which are to be expected for a stiff site.
As for the traces collected by the sensors of the passive array, these were manually identified in the microtremor recordings and processed separately from noise data. In this case the sampling frequency is the same of the passive data, 200 Hz.

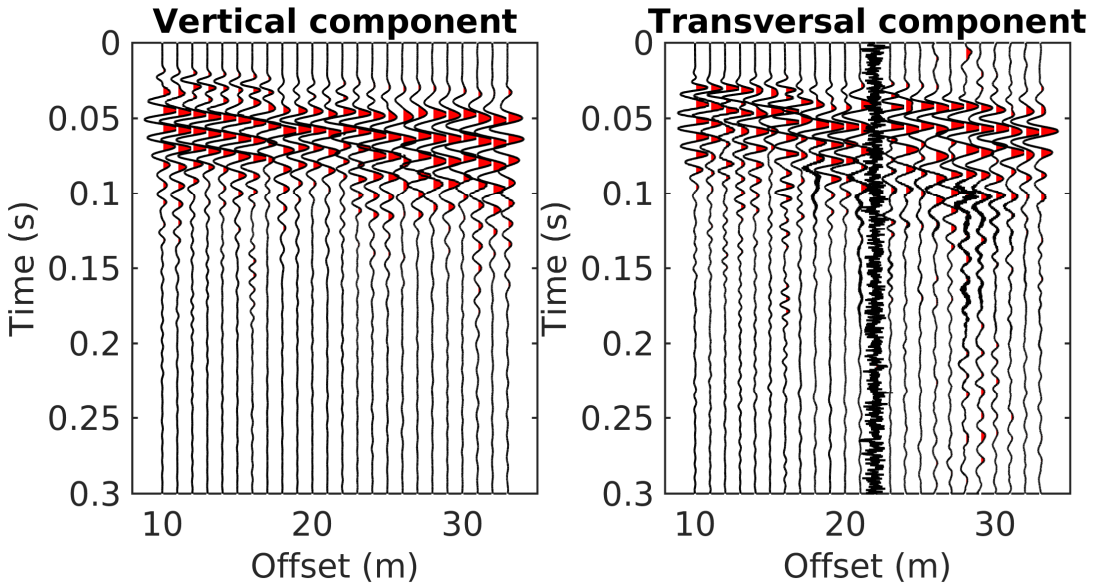

Figure 8 – Two sample seismic sections acquired by the geophone array, with shooting position at scr2. Left: vertical component traces generated by a vertical blow of the hammer on the flat plate. Right: transversal component traces generated by hitting the wedge plate on one of its two sides. One of the traces (offset = 22 m) is clearly faulty and was removed from the following processing operations

5. Data processing

Data acquired in the active and passive surveys were processed in order to determine the characteristics of propagation of surface waves (passive array acquisition) and surface and P-waves (active acquisitions).

5.1 Passive data processing

5.1.1 H/V analysis

The seismic data (three-component traces) acquired by each sensor of the passive array were processed with:

- classical H/V techniques (as implemented in Geopsy software, www.geopsy.org; classical H/V of Fäh et al., 2001), determining the spectral ratio between horizontal and vertical components (Nakamura, 1989), whose peaks are related to the frequencies of resonance of the site;
- more refined algorithms, estimating the ellipticity of Rayleigh wave as a function of frequency (RayDec, Hobiger at al., 2009; time-frequency method, Poggi and Fäh, 2010; wavelet-based time-frequency method as implemented in Geopsy software). These methods aim at eliminating the contributions of other waves besides Rayleigh waves, to obtain a more reliable estimation of Rayleigh wave ellipticity when compared to the classical H/V technique.

Figure 9 shows the results obtained from different techniques for 8 sample receivers; Figure 10 displays the H/V curves derived applying the time-frequency method of Poggi and Fäh (2010) at all stations, on which the fundamental frequency values and also a second peak frequency were picked.

The various techniques yield consistent results (Figure 9). In terms of spatial variability, a similar behaviour is observed at almost all receivers, with curves without pronounced peak as it is expected for a stiff site.

The picked values for the fundamental frequency f_0 (Figure 10) lie between 0.61 and 0.69 Hz for all stations. The second peak shows more variation and lie mostly between 1.99 and 2.33 Hz, with three stations having lower peak frequencies of 1.39, 1.75 and 1.83 Hz, respectively. These outliers correspond to the stations along the first ring of the passive array (radius = 5.2 m). It is worth noting that the H/V curves from these sensors exhibit also spectral ratio values that are considerably higher when compared with the curves from all other stations (Figure 10). Both anomalous features (lower second peak, higher spectral ratios) cannot be observed in the neighboring stations (sensors along the second ring and at the center of the array), so that it is possible to explain this atypical behavior with local disturbances (e.g. the effect of trees or underground cables, or imperfect coupling).

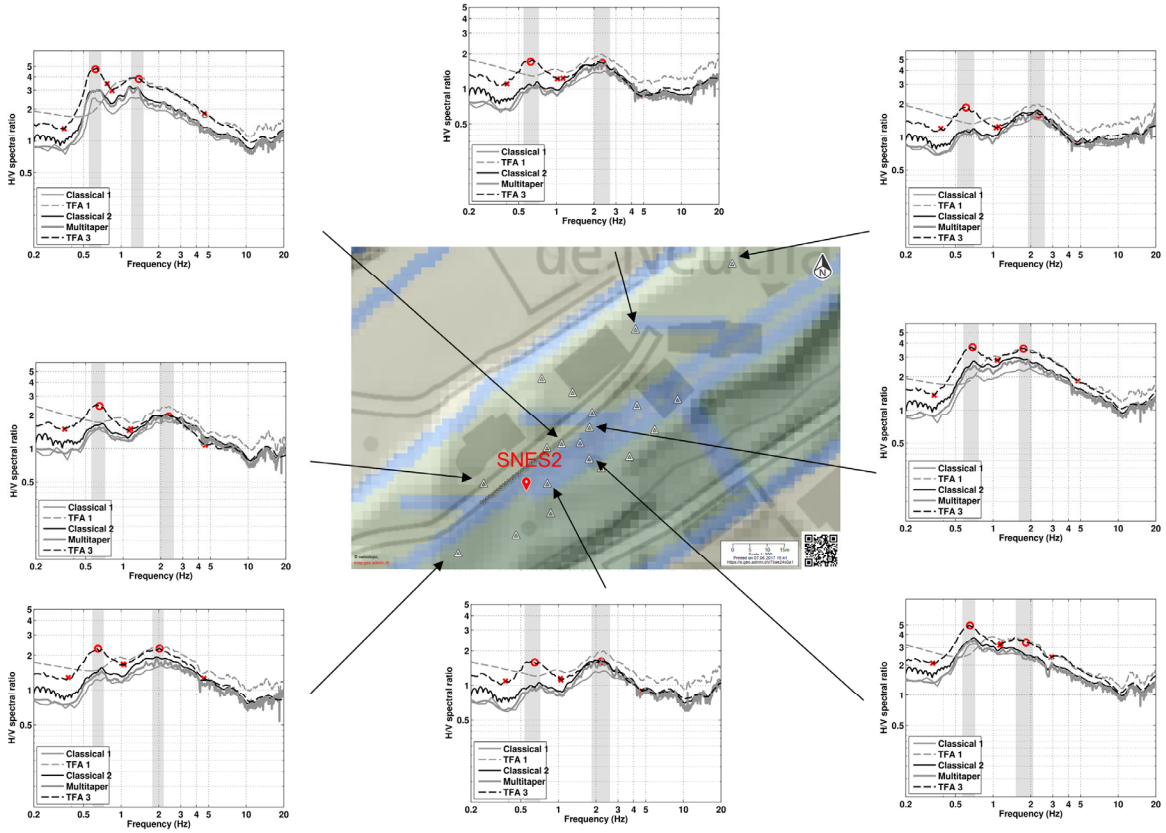

Figure 9 – H/V analysis. The insets surrounding the map of the passive array contain the H/V curves for some sample locations. Classical 1: Geopsy; Classical 2: Fäh et al., 2001; TFA1: wavelet-based time-frequency method as implemented in Geopsy software; TFA3: time-frequency method, Poggi and Fäh, 2010. The map in the center of the figure represents the local surficial geology (according to the 1:25000 Swiss geological atlases, © 2019 Swisstopo, JD100042; see figure 14a for color codes), superimposed to the digital elevation model for the area.

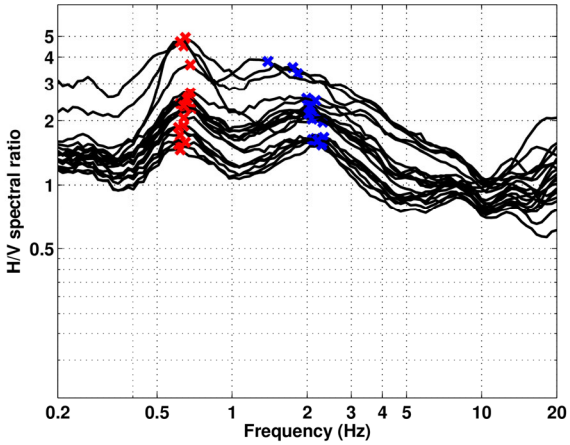

Figure 10 – H/V curves from all passive sensors, obtained applying the time-frequency method, Poggi and Fäh (2010; TFA3 in Figure 6). The picked values for the fundamental frequency are represented as red crosses, the second peak frequency as blue crosses.

5.1.2 Polarization analysis

The single-station recordings from the passive array were also processed with the polarization tool of Burjánek et al. (2010). In Figures 11 and 12 we display the produced ellipticity (as defined in Burjánek et al., 2011) and strike graphs as a function of frequency for the same sample stations of Figure 9. The ellipticity plots (Figure 11) generally show only very weak troughs at the H/V peak frequencies of around 0.65 and 2.2 Hz, and also at frequencies above 10 Hz for some stations. This second feature is associated with high values of relative occurrence in the strike plots in the same frequency band (Figure 12), along the north-west/south-east axis. This direction is perpendicular to the main axis of the ridge where station SNES2 is located, suggesting that this feature might point out the resonance frequency of this topological feature. This aspect is discussed quantitatively in the interpretation of the retrieved velocity profiles (section 7).
As observed in the H/V analysis (see previous section, Figure 9), the sensor whose ellipticity and strike plots are displayed in the upper left corner (Figures 11, 12) exhibits a pattern different from that of all other receivers, with a more pronounced polarization pattern at the H/V peak frequencies in the north-east/south-west direction.

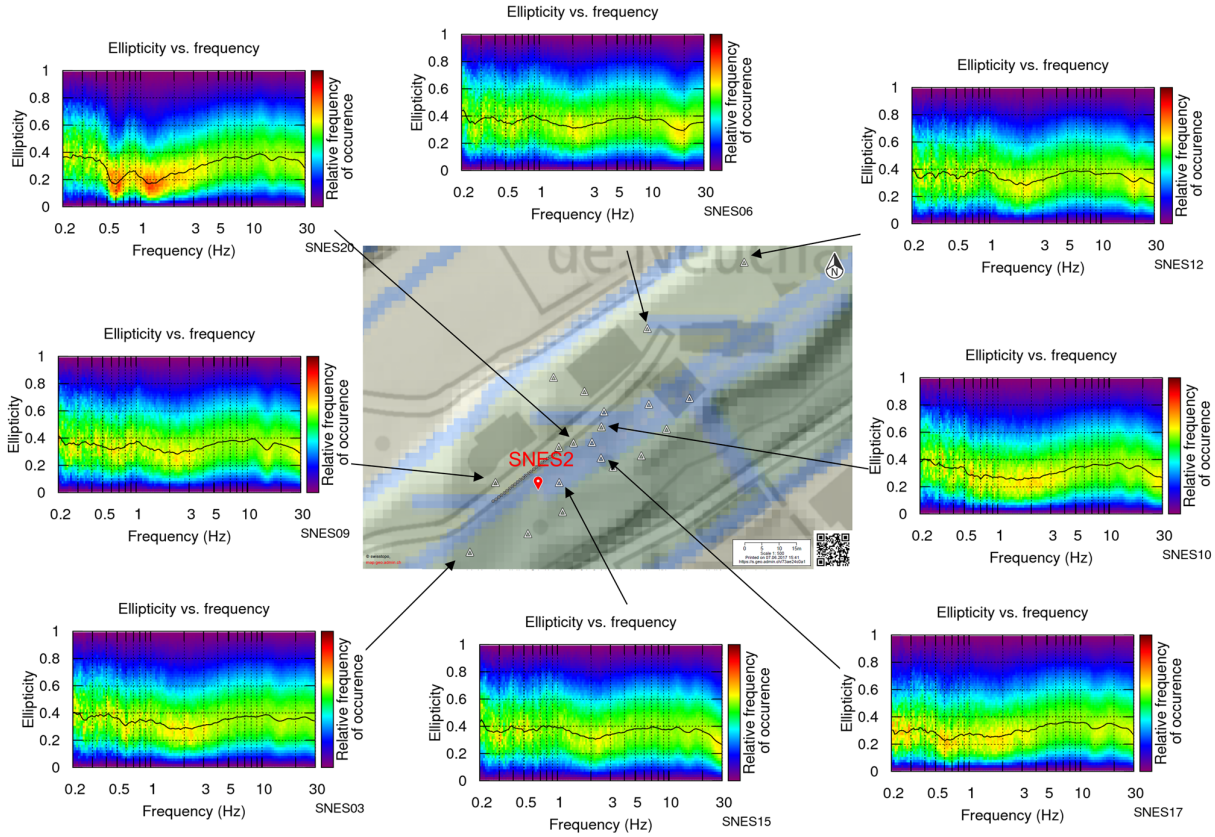

Figure 11 – Polarization analysis. Ellipticity vs frequency graphs from some samples receivers of the passive array.

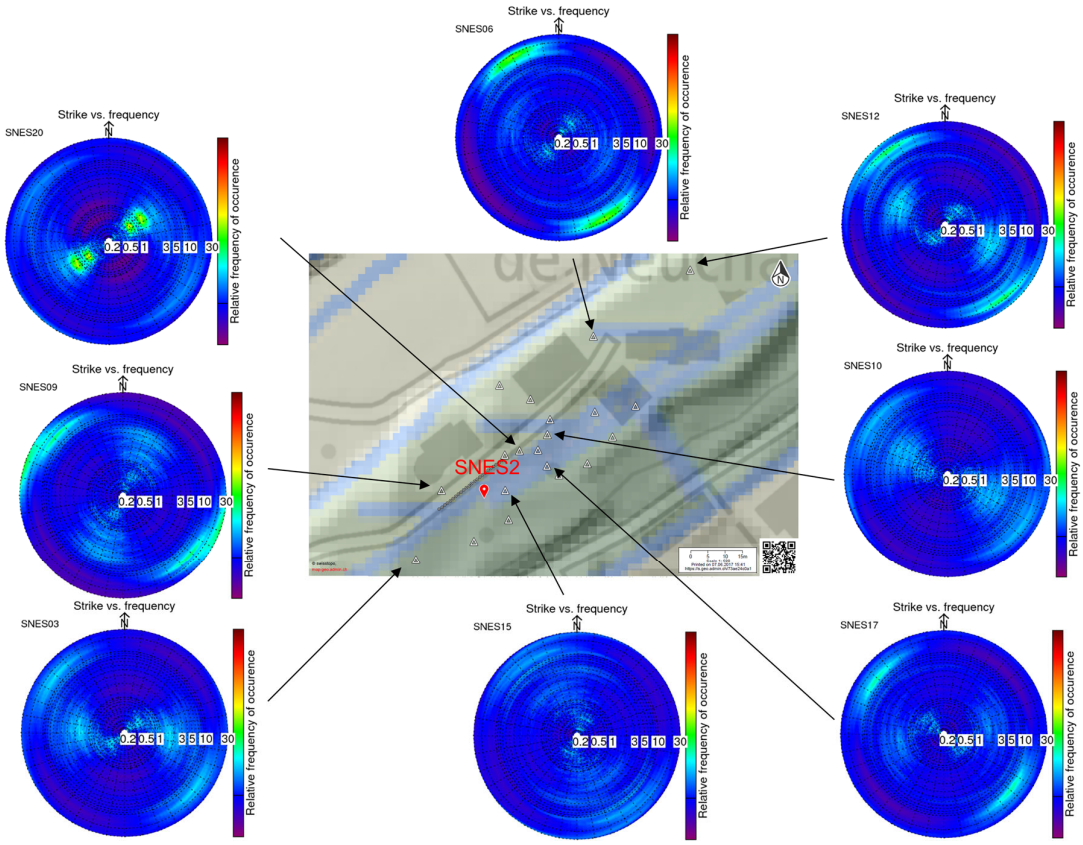

Figure 12 – Polarization analysis. Strike vs frequency graphs from some samples receivers of the passive array.

5.1.3 Three-component high-resolution f-k

Besides the single-station procedures illustrated in the previous sections, the multi-component microtremor recordings from the passive array were jointly processed to derive the properties of propagation of surface waves (frequency-dependent phase velocities for both Love and Rayleigh waves, ellipticity values for Rayleigh waves). The adopted method is the three-component high-resolution *f-k* analysis (Poggi and Fäh, 2010). The obtained results are illustrated, component by component, in Figure 13.

Because of the limited available space on the ridge, the passive seismic array has a very narrow resolution limit. Actually, the lowest resolvable wave length k_{min} has a value of 0.091 m^{-1} (as determined using the warangps function of the geopsy package). This means that, for example, at 10 Hz no wave velocities higher than 692 m/s can be resolved. The largest resolvable wavelength of the array is determined as k_{max} = 7.7 m^{-1}. As can be seen in Figure 13, the wave velocities at the site are rather high and we can therefore only resolve seismic velocities above 20 Hz. The passive array would be capable of resolving waves to frequencies around 100 Hz, but unfortunately, these waves in the natural ambient vibrations do not have much energy and we can only measure wave velocities in a very narrow range.

On the vertical component, we can determine a dispersion curve between 25.6 and 38.1 Hz, while on the radial component, we can identify it between 28.2 and 32.8 Hz. Both components are related to the Rayleigh wave propagation.

On the transverse component, which is related to the Love wave propagation, two different dispersion curves are identified, which are however close to each other, so that they might also be only one curve. The first is picked between 28.2 and 36.3 Hz, the second one between 29.7 and 36.3 Hz.

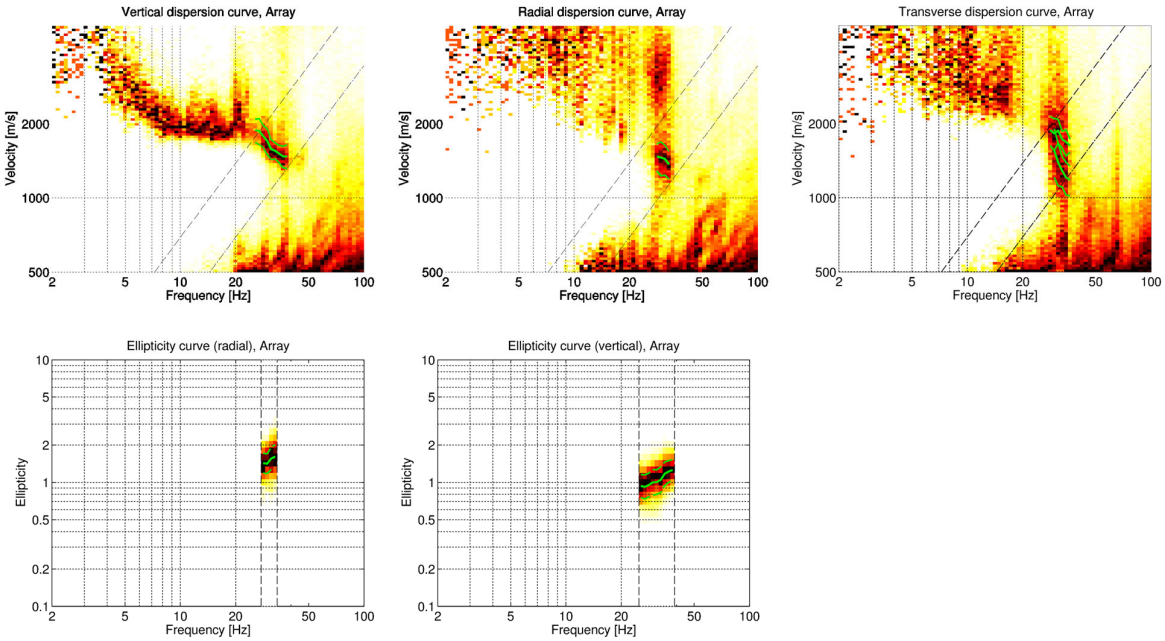

Figure 13 – Three-component high-resolution f-k: processing results for the vertical (left), radial (centre), and transverse component (right). Top: phase velocity estimates. Bottom: Rayleigh wave ellipticity estimates. The density of the estimates in the velocity (or ellipticity) vs frequency planes is represented with the yellow-to-black color scale. The picked curves are in green, together with the standard deviations. The dashed black lines indicate the lower resolution limits of the array, where the left line corresponds to $k_{min} = 0.091\ m^{-1}$ *and the second line to 2* k_{min}*. The higher resolution limits are outside of the plot limits.*

5.2 Active data processing

5.2.1 Refraction processing

The vertical-component seismic traces recorded by the geophones and generated with the source positioned at scr1 or src4 (the two shooting positions closer to the geophone array, see Figure 6) were summed – or stacked – in time domain. This was done to enhance the coherent seismic events generated by the controlled seismic source, and at the same time to minimize the incoherent noise anyhow present in the recordings (Foti et al., 2015). To preserve the effectiveness of the stacking operation, the vertical components of the seismic traces at short offsets were cross-correlated to ensure a robust synchronization among the seismograms to be later superimposed. P-wave first break arrivals were hence manually picked on these two "stacked" seismic sections (one from src1 and one from src4, see Figure 14a). The two travel-time curves (Figure14b) are approximately symmetrical (or identical in time-offset domain, Figure 14c) for source-receiver offsets of less than 12 m. Beyond this value, the travel-times from src4 are larger than their src1 equivalent, although it is not possible to determine whether this discrepancy corresponds to an actual feature in the subsurface, or the

manual picking missed the first arrivals. Therefore, only the portion having offsets below 12 m was interpreted (Figure 14c) with the intercept time method (Reynolds, 2011), yielding the surficial V_P model of Figure 11d.

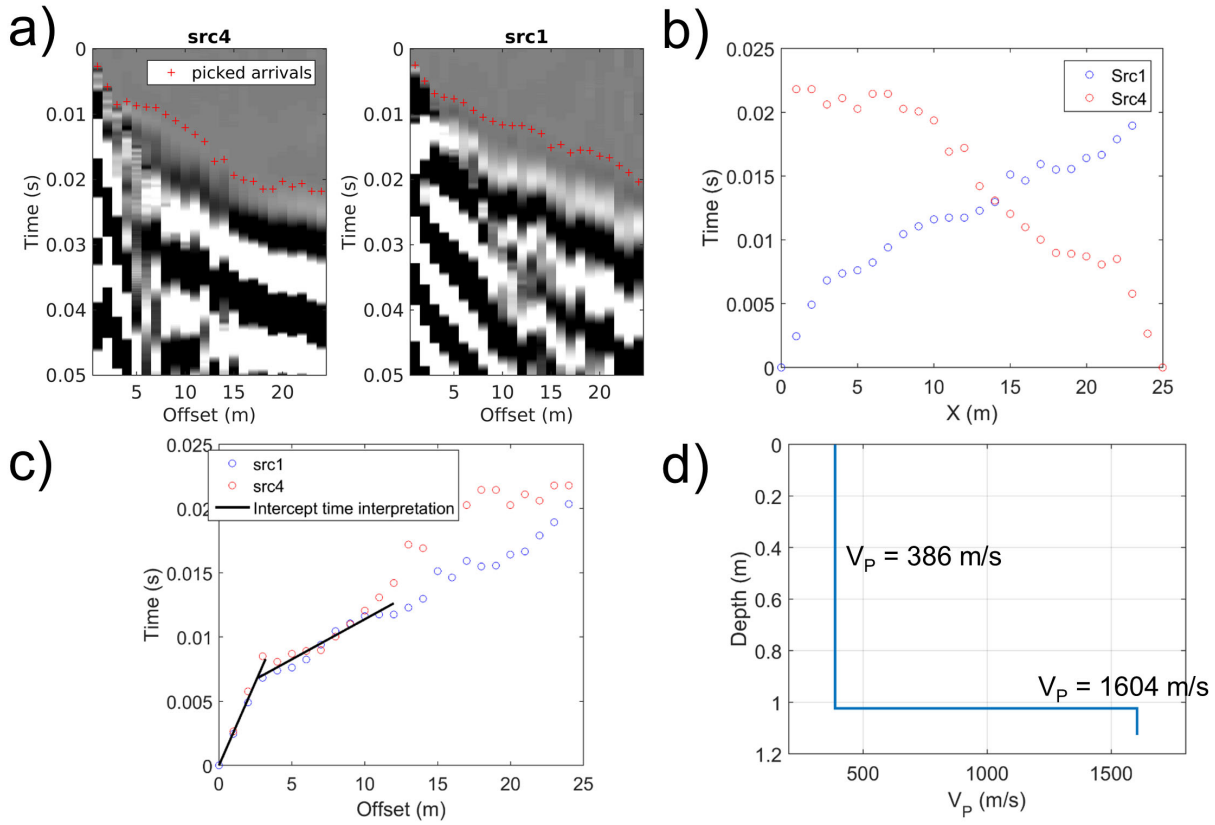

Figure 14 – P-wave refraction processing. a) Picking of P-wave first break arrival times; b) obtained hodocrones. c) intercept time interpretation; b) derived shallow V_P model.

5.2.2 MASW processing of geophone data

The vertical and radial component traces acquired by the geophone line for hammer shots on the flat plate positioned at src2 or src5 (see Figure 6), were processed with conventional *f-k* processing (Socco and Strobbia 2004) to obtain Rayleigh wave dispersion curves. Single-shot seismic sections are first translated from time-offset to frequency-wavenumber domain using a 2D Fourier transform; the *f-k* panels referring to the same recording component and source position are then stacked to obtain *f-k* images with higher signal to noise ratio. Their energy maxima are then picked by defining manually areas of interest on the spectral image, then identifying automatically the maxima frequency by frequency (Figure 15, left).

The main feature in the *f-k* panels is a poorly dispersive feature with velocities around 1600 m/s (see white line in the panels in Figure 15, left); this is probably a P-guided mode traveling in the layer whose V_P = 1604 m/s was determined thanks to P-wave refraction (Figure 14d). As the inversion of surface wave data will later show (Figure 18), this layer is bounded at its lower interface by a high impedance contrast, a condition that favors the onset of guided waves. At lower velocities, we picked

less energetic dispersive features that show a good reciprocal consistency (Figure 15, right panel) and depict several branches in the frequency-phase velocity plane. Since these points show a consistent and definite trend even past the maximum-wavelength array limit (conventionally set to twice the array length, Figure 5, right), the picked curves extend down to about 20 Hz.

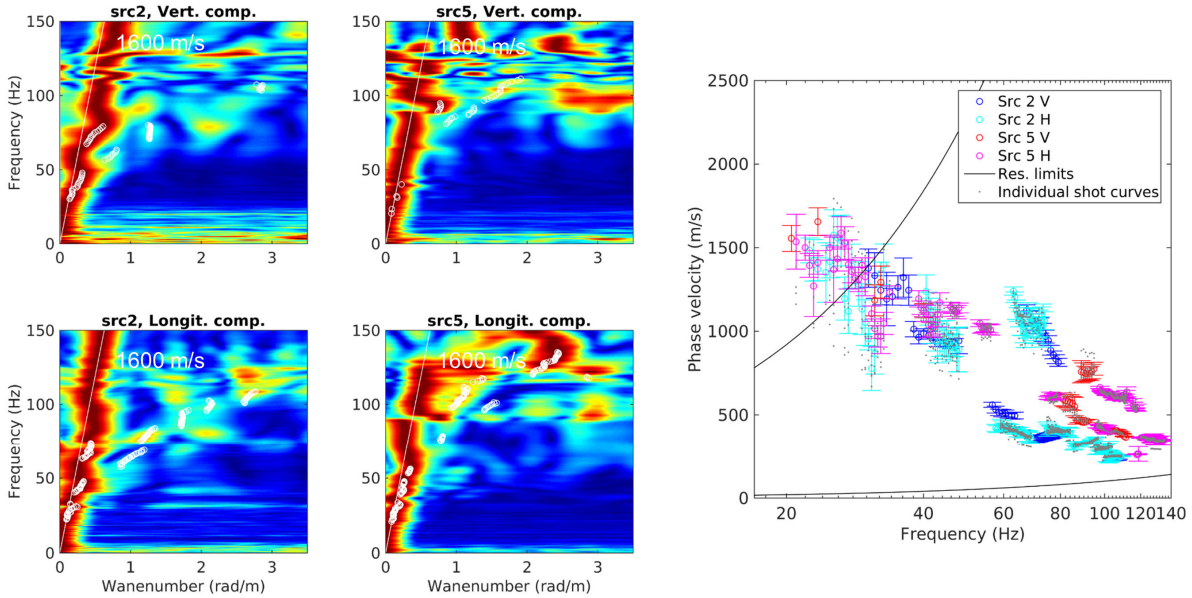

Figure 15 – MASW processing of geophone data. Left: stacked f-k panels obtained from either vertical- (top) or radial- (bottom) component traces, the source position being either src2 (left) or src5 (right). Picked maxima are represented as white circles. The white line corresponds to a velocity of 1600 m/s, which fits quite well with the most energetic feature in the panels. Right: picked Rayleigh wave dispersion curves; the minimum and maximum observable wavelength (black lines) are set to the inter-geophone distance and to twice the total array length, respectively.

At this stage of the processing, it was not possible to determine the Rayleigh wave mode of the picked branches. Therefore, to attribute the obtained data points to defined Rayleigh wave propagation modes, a preliminary inversion was run using the Monte Carlo inversion tool of Maraschini and Foti (2010). The code performs a purely random search in the parameter space, using as misfit function the values of the absolute determinant of the transfer matrix evaluated at the frequency-phase velocity coordinates of the experimental data points. Hence, the code does not require mode numbering but it attributes itself the experimental points to a given mode, looking for the lowest misfit solution. The best fitting absolute determinant surface, out of a total population of 600 000 randomly generated models, is shown in Figure 16 (left). Data points are attributed to the fundamental, first and second higher Rayleigh wave propagation mode (Figure 16, left). After this mode numbering stage, curves from different source positions (src2 and src5) and recording components (vertical, radial) were collapsed through averaging in a single Rayleigh wave dispersion curve (Figure 16, right panel). The fitting with the Rayleigh wave curves from passive data (section 5.1.3) is quite poor, as these exhibit higher phase velocities. Two reasons can be proposed to explain this disagreement:

- In contrast to the geophone line, the passive array was deployed on an area spanning two different geological covers, according to the local geological atlas. This geological discontinuity might explain the different values of phase velocity (Figure 17a).

- The passive array sensors were deployed at various altitudes on an area with pronounced topography (an elongated ridge). As shown by Zeng et al. (2012), marked topographical features might produce an apparent dispersion curve that deviates significantly from the curve that one would get in a 1D situation. Due to the location on the ridge, directional effects of wave propagation might also play a role.

Therefore, the curves from the three-component high-resolution *f-k* processing of microtremor data were discarded from the successive inversion stage.

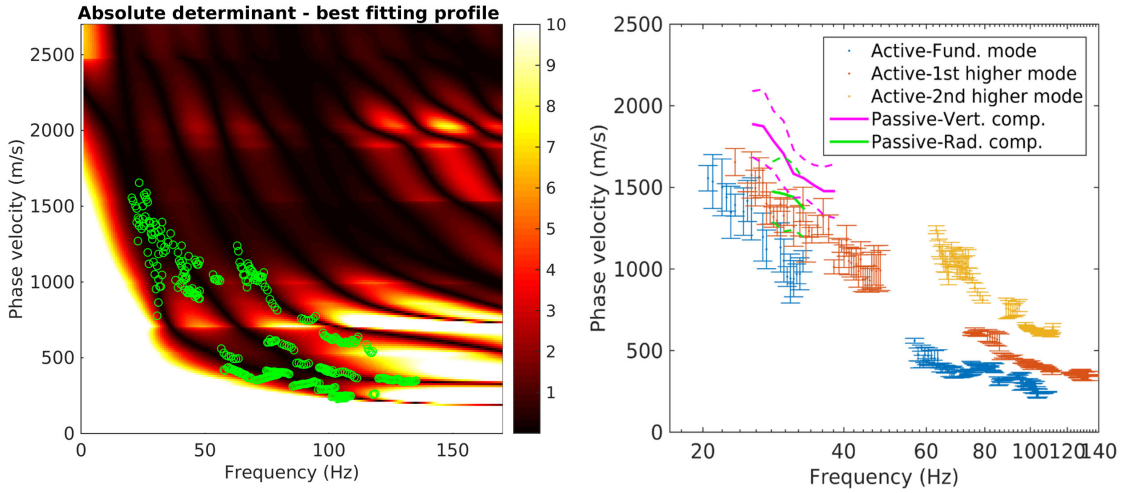

Figure 16 – MASW processing, Rayleigh waves. Left: best fitting absolute determinant surface determined by Maraschini and Foti (2010) Monte Carlo approach (colored background); the green circles are the multimodal Rayleigh wave dispersion curve obtained from geophone data (Figure 12, right plot). Right: Rayleigh wave dispersion curve obtained from geophone data with modal attribution, collated with the picked curves from passive data (Figure 10).

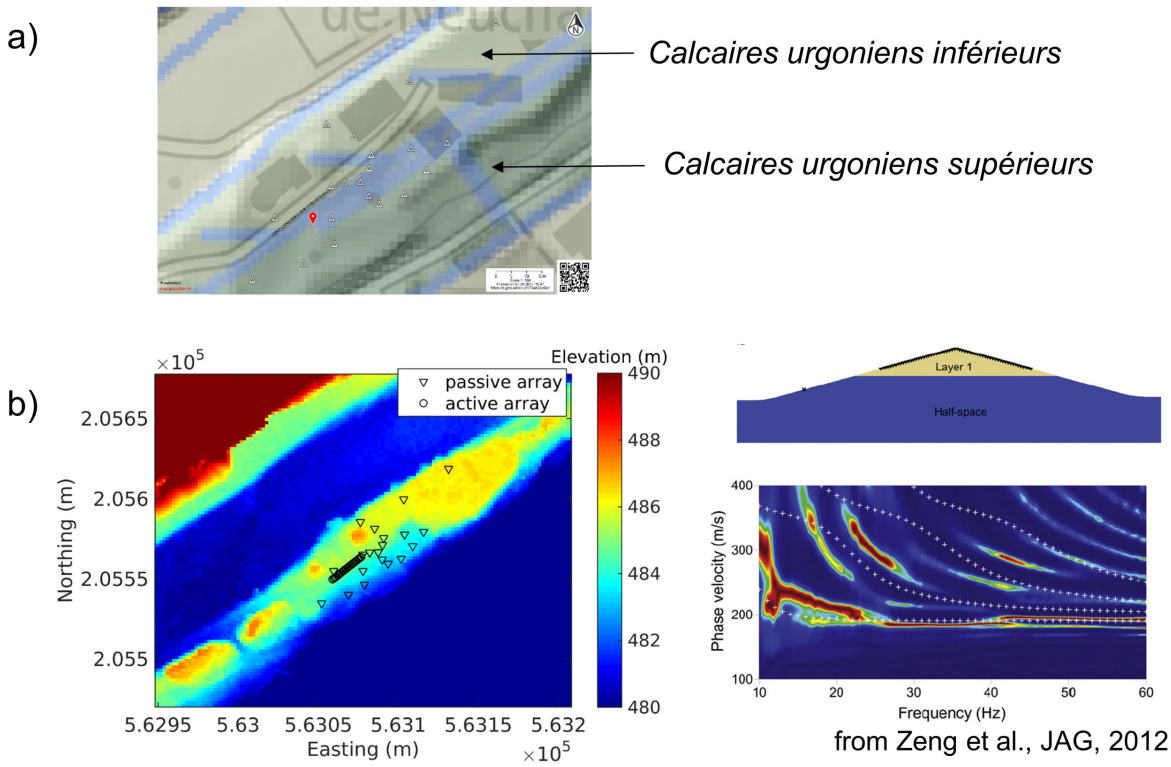

Figure 17 – Possible reasons for the mismatch between dispersion curves obtained from the passive array and the geophone line: a) Presence of a lateral geological discontinuity: the passive array was deployed across the border between two types of outcropping rock. b) Topography effects. The passive array was deployed on a narrow, elongated ridge, with sensors at different altitudes (left inset). As shown in the paper of Zeng et al. (2012; right panel), this recording configuration might not correspond to the assumption of 1D surface wave propagation.

For the extraction of Love wave dispersion curves from the geophone data, we used the traces recorded using as active source the hammer hitting the wedge plate (see section 4.2). In fact, the hammer blows exerted on the slant faces of the wedge apply a two-component excitation to the ground: a vertical and a horizontal component, the direction of the latter depending on which face of the plate the stroke is given. Therefore, by summing the seismic traces obtained hitting the wedge on the two sides, the effects of the horizontal components are mutually eliminated, while the vertical components interact constructively; by computing the difference of the corresponding seismograms, the vertical components nullify each other, while the horizontal components interact constructively (Schmelzbach et al., 2016; Sollberger et al., 2016). Consequently, the sum operator is equivalent to the use of a vertical blow; the difference operator is equivalent to a pure shear source.

Therefore, for the extraction of Love wave dispersion data, 2D *f-k* analysis was applied to the seismograms obtained as the sum (i.e. stack) of the differences between the transversal-component traces acquired when alternately hitting the two opposite faces of the wedge-shaped plate (Figure 18, left panels; these seismic sections should portray a purely SH excitation). In this case, the stacking operation was performed, similarly to P-wave refraction and differently from Rayleigh wave processing, in time-offset domain. In fact, to reproduce the effect of an SH source, the difference operation presupposes similar spectral energy content between the seismic recordings that are subtracted; this assumption is indeed more robust when considering altogether (through a stacking

operation) the single-shot seismograms. The central plots in Figure 18 show the *f-k* panels obtained from the two shooting positions suitable for MASW (Love) analyses (src2 and src5, see Figure 6), as well as the picked energy maxima. The two picked curves (Figure 18, right plot) show some consistency above 30 Hz, while at lower frequencies their trend is not clear. For the inversion process (see next section), we retained the branch extending between 30 and 90 Hz, exhibiting the lowest velocities and therefore identified as fundamental mode. Similarly as observed for Rayleigh waves, the curves from passive data (Figure 18, right panel) show higher velocities than those obtained from geophone data: they were not included in the inversion target.

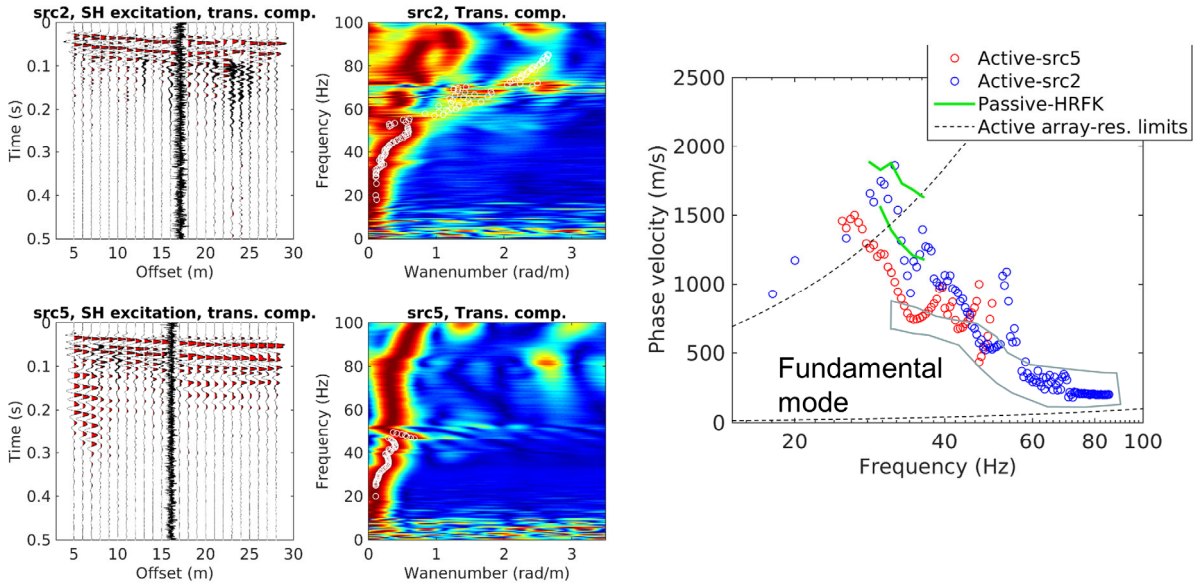

Figure 18 – MASW processing, Love waves. Left: seismic sections obtained for source positions src2 (top) and src5 (bottom) subtracting the transversal-component traces generated by hitting the wedge plate on its two sides. Center: f-k panels obtained applying a 2D Fourier transform to the seismic sections in the left. Picked energy maxima are represented as white circles. Right: obtained Love wave dispersion curves (red and blue circles) collated with the dispersion curves from passive data (green lines: see also Figure 13, top-right panel). The portion identified as fundamental mode is highlighted with a light-blue polygon.

5.2.3 Wavefield decomposition of active data

For comparison and completeness of analysis, we processed the geophone data and the active traces acquired by the passive array with the WaveDecActive code (Maranò et al., 2017).
WaveDecActive implements a maximum likelihood algorithm for the analysis of Rayleigh waves generated by a controlled source. Differently from the more conventional *f-k* analysis approach (see previous section), it is able to characterize the Rayleigh wave propagation both in terms of phase velocity and ellipticity angle, as it processes jointly all acquired components. Key parameters required by WaveDecActive are the definition of the maximum number of Rayleigh waves that the code attempts to identify, and the value of the parameter γ, which is able to modify the approach of the

code towards wave identification from a Bayesian information criterion ($\gamma = 1$) to a maximum likelihood approach (ML, $\gamma = 0$), or a compromise between the two ($0 < \gamma < 1$). Following the recommendations of the code's author (Maranò, 2016) and some preliminary attempts, the maximum number of waves was set to 3, and γ to 0.3, thus opting for an approach relatively close to a maximum likelihood solution.

The obtained results are displayed in Figure 19, showing the estimated Rayleigh wave phase velocities from the traces recorded by the geophone array (top panel; source positions src1, src2, src4, src5) and the passive array (bottom panel; all 9 shooting positions were considered). The information regarding the estimated ellipticity angle is expressed by the color scale. The two plots contain a high number of outliers, as well as features in agreement with the Rayleigh wave dispersion curves from *f-k* processing (black dots). As observed in other cases (Bergamo et al., 2017), the WaveDecActive processing technique does not perform very well at stiff sites.

To conclude, it is possible to affirm that the surveyed site (stiff site with marked topography) does not favor surface wave data acquisition. Active data acquired with the geophone line and processed with the *f-k* method provide results with some consistency that were passed on to the successive inversion stage.

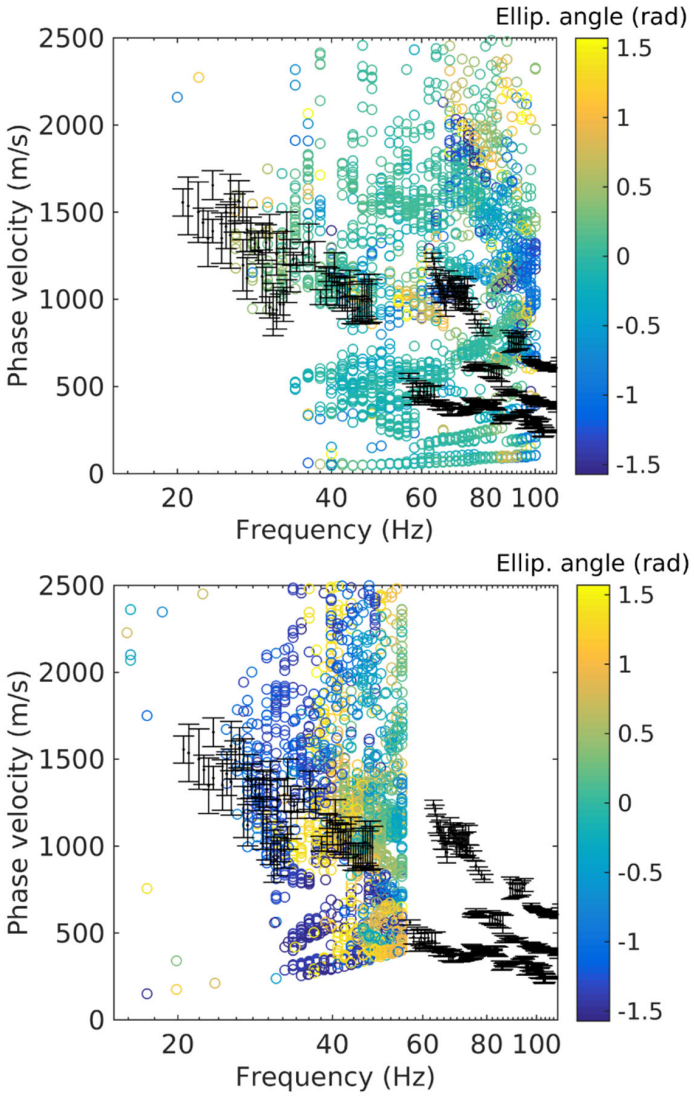

Figure 19 – WaveDecActive processing results. Estimated phase velocities (circles) obtained from the processing of geophone data (top) and active traces recorded by the passive array (bottom). The corresponding ellipticity angle is reported in color scale. The Rayleigh wave dispersion curve derived from the f-k analysis of geophone data is represented for comparison in both plot, with black dots.

6. Surface wave data inversion

The inversion of surface wave data for the VS profile at station SNES2 was carried out using the *dinver* software from the Geopsy suite, which implements an Improved Neighbourhood Algorithm (Wathelet, 2008) for the search of the best fitting parameters.

6.1 Inversion target

The curves included in the target for the inversion process are:

- the multimodal Rayleigh wave dispersion curve obtained from active geophone traces processed with *f-k* analysis (section 5.2.2, Figure 16, right plot);
- the fundamental mode of the Love wave dispersion curve derived from active geophone traces processed with *f-k* analysis (section 5.2.2, Figure 18, right plot);
- the ellipticity curve obtained from the single-station, passive recordings of the passive array sensor closest to SNES2, processed with the RayDec code (Hobiger et al., 2009). Its consistency with other ellipticity estimates from the same data was checked (see Figure 6, bottom center inset). The curve was attributed to the fundamental mode of Rayleigh wave propagation. It is represented in Figure 20. After a number of preliminary inversion trials, it resulted impossible to fit both the dispersion curves (Rayleigh, Love) and the ellipticity curve (which probably does not belong entirely to the fundamental mode). Therefore, the ellipticity curve was excluded from the RMS error computation of the final inversion runs (see following sections).

All curves include their uncertainty intervals. Both ellipticity and dispersion curves were resampled using 200 points between 1 and 135 Hz, on a logarithmic scale.
As already explained in section 5, the dispersion and ellipticity curves from microtremor data recorded by the passive array were not considered for the inversion, as they might be affected by lateral discontinuities or topographical effects (Figure 17).

6.2 Parameterization of the model space

The subsurface was parameterized as a stack of 5 homogeneous layers, overlying a half-space. Their velocities (V_P, V_S) and thickness values were left free to vary within predefined intervals. For the two uppermost layers, the range of possible velocities was narrowed down thanks to the P-wave refraction results (section 5.2.1); this applies also to the thickness of the top layer. Poisson's ratios were set to vary within 0.2-0.4 for the uppermost layer, and gradually reducing their interval with depth down to 0.2-0.3 for the half-space. The values of bulk densities for each layer were assigned, increasing with depth from 1600 kg/m^3 (most surficial layer) to 2300 kg/m^3 (half-space).
We ran 20 inversion processes (i.e. having the same inversion target and parameterization) to obtain as many velocity profiles (the best performing model from every process). In each inversion run, 200 000 randomly generated models are initially tested: the successive refinement stage involves 100 iterations, each with the test of 1000 newly generated models. The achieved minimum misfits (RMS error) vary within the range 1.36-1.39.

6.3 Inversion results

Figure 20 shows the results from the inversion run obtaining the minimum misfit of 1.36.As anticipated, the fitting of the multimodal Rayleigh wave dispersion curve (top of Figure 20) is good; for Love waves, the modeled phase velocities below 40 Hz are higher than those from experimental data. In Figure 20, we also show the Rayleigh wave ellipticity curve, which does not contribute to the final misfit (RMSE); the synthetic ellipticities are higher than the experimental ones across all the frequency band, and it is possible to conclude that the latter does not belong entirely to the fundamental mode (as supposed for the inversion target).

The best-performing velocity profiles (bottom row in Figure 20) define a consistent trend, thus showing a convergence to a common solution.
The 20 lowest-misfit models from each of the 20 inversion runs are represented in Figure 21; they are described and commented in the following section.

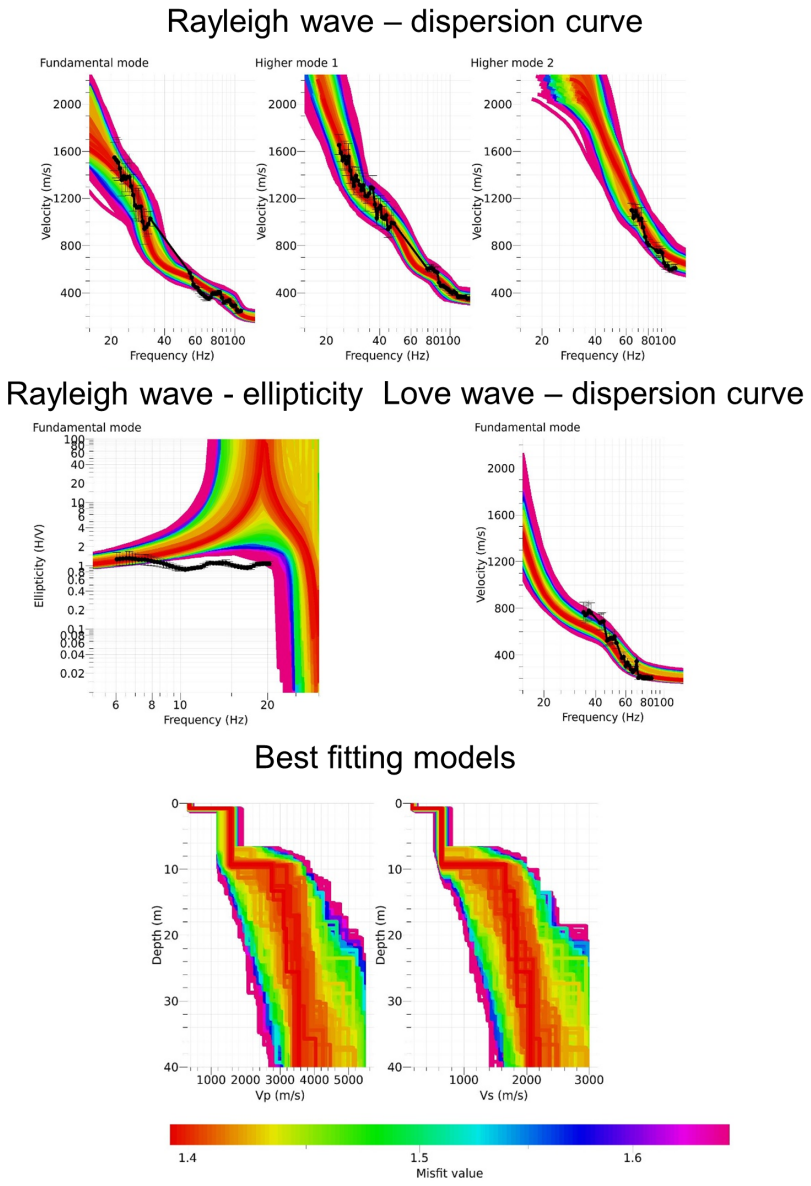

Figure 20 – Results from the inversion process with the lowest misfit. Top: comparison between experimental (black dots) and synthetic Rayleigh wave dispersion curves (colored lines: see bottom of the figure for the color scale). Centre: same comparison for Rayleigh wave ellipticity (not included in the computation of the final RMS error) and Love wave dispersion curve. Bottom: best fitting V_P (left) and V_S (right) profiles.

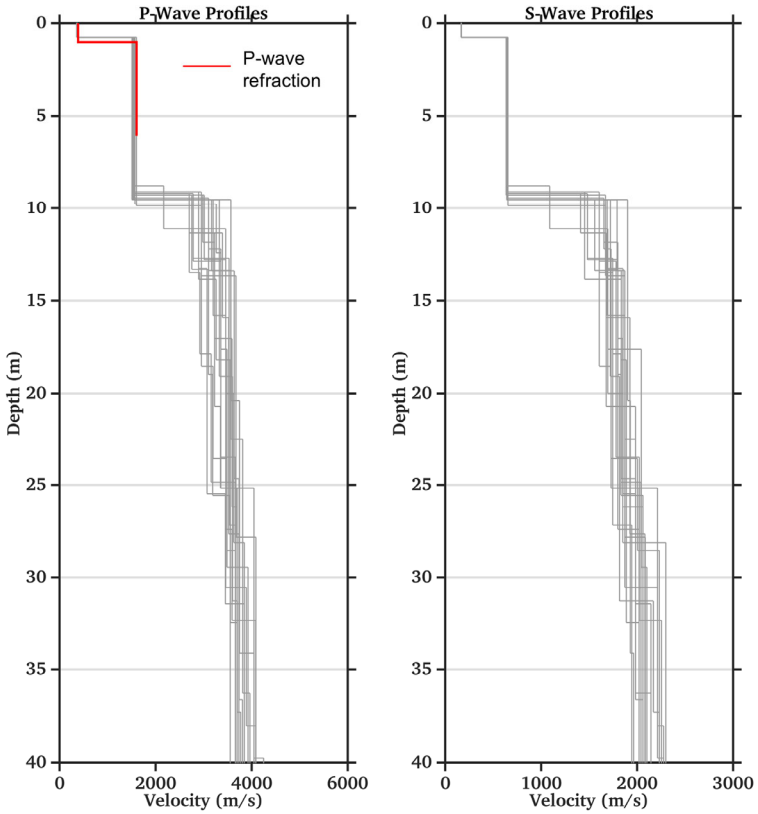

Figure 21 – Best performing models (V_P and V_S profiles) from each of the 20 parallel inversion runs. The surficial V_P model from refraction is shown in blue (right inset).

7 Interpretation of the inversion results

7.1 Velocity profiles

Figure 21 displays the 20 lowest misfit models from each of the 20 inversion runs. Below a thin layer of soil cover (thickness of about 0.75 m, V_S = 167 m/s), a relatively stiff formation with S-wave velocity of 635 m/s and thickness of 8.4 m is found. It is possible to argue that this formation, probably moraine, is the main material forming the ridge of the Neuchâtel Observatory (Figure 17; its thickness at SNES2 is approximately the height of the ridge).
Assuming this velocity value (V_S = 635 m/s), it is possible to compute the resonance frequency (f_0) of the ridge, with the formula proposed by Géli et al. (1988):

$$f_0 = 0.4\frac{V_S}{L} \quad (1)$$

where L is the semi-width of the ridge (around 40 m).
The obtained value of f_0 (12.7 Hz) corresponds quite well with peaks of the strike-frequency plots (Figure 12), showing a marked directionality in the direction orthogonal to the ridge main axis.
Below the second layer (about 9.5 m deep), we find a significant increase in V_S and V_P (which become about 1600 and 3000 m/s, respectively): this is the upper interface of the bedrock (probably degraded

limestone at this depth). Both V_S and V_P then gradually increase with depth, reaching around 2000 and 3600 m/s, respectively, at 30 m.

7.2 Quarter-wavelength representation

The quarter-wavelength velocity representation (V_S^{QWL}; Joyner et al., 1981) attributes to each frequency the average velocity at a depth equal to ¼ of the corresponding wavelength. V_S^{QWL} can be used as direct proxy for the local site characterization, as it physically relates the resolution on ground parameters with the characteristics of the propagating wave-field at discrete frequencies. The derived quarter-wavelength impedance contrast (IC^{QWL}; Poggi et al., 2012) is the ratio between two quarter-wavelength average velocities, from the top and bottom part of the velocity profile respectively, at a given frequency; it is a powerful tool to assess the influence of resonance phenomena in soft sediment sites.

Figure 22 shows the average (over the population of the selected 20 best subsurface models) quarter-wavelength velocity (center) and impedance contrast (bottom) representations. The obtained V_{S30} (which is the average velocity corresponding to a quarter-wavelength of 30 m) is 1021 m/s.

The IC^{QWL} graph shows a peak at 15 Hz, which is related to the interface between the upper moraine and lower bedrock (limestone) formation at around 10 m depth (Figure 21).

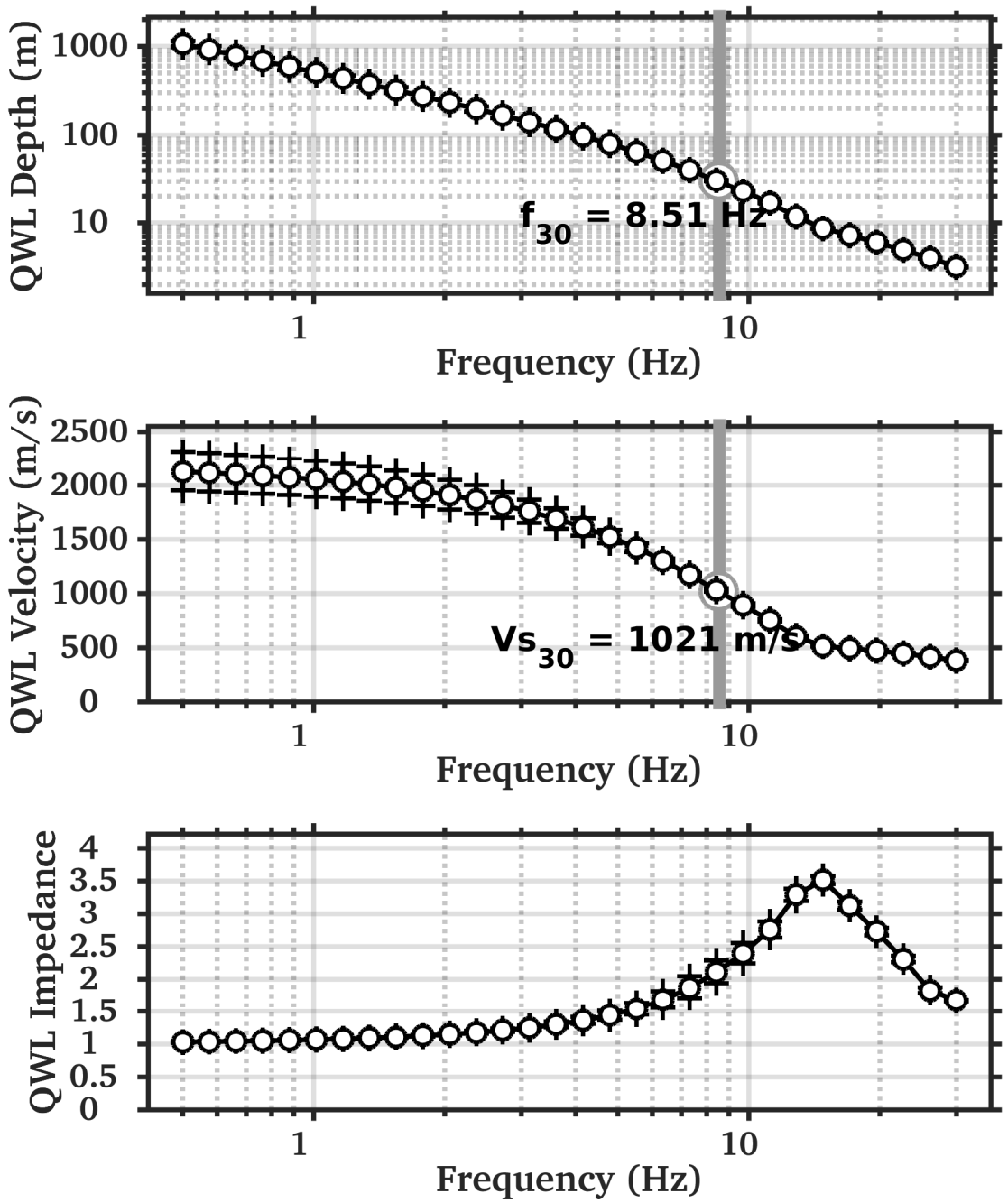

Figure 22 – Average quarter-wavelength representation of the selected velocity profile. Top: depth; center: velocity; bottom: impedance contrast. The gray line in the top and center panel refers to V_{S30}.

7.3 SH transfer function.

The theoretical SH-wave transfer functions for vertical propagation (Roesset, 1970) were computed for the selected models (Figure 23). The transfer functions are then corrected for the Swiss reference rock model (Poggi et al., 2011), following Edwards et al. (2013).
These are compared with the empirical amplification function obtained from spectral modeling (ESM,; Edwards et al., 2013; Michel et al., 2014), relying on 40 events in the central 2.5 – 14 Hz frequency band, decreasing to 10 events at lower and higher frequencies (as of 4 April 2017). The modeled and empirically-derived functions agree in defining substantially flat graphs (low values of amplification, also below 1), which are expected for such a stiff site. The peaks of the synthetic functions (around 16 Hz) are related to the impedance contrast at the upper interface of the bedrock (Figure 21), in a 1D assumption for the geometry of the site. The peak observed in the empirical amplification function is slightly lower (around 13 Hz), and can be related to the resonance frequency of the ridge where station SNES2 is located (see section 7.1). Clearly, this feature cannot be modeled by the synthetic SH-transfer function.

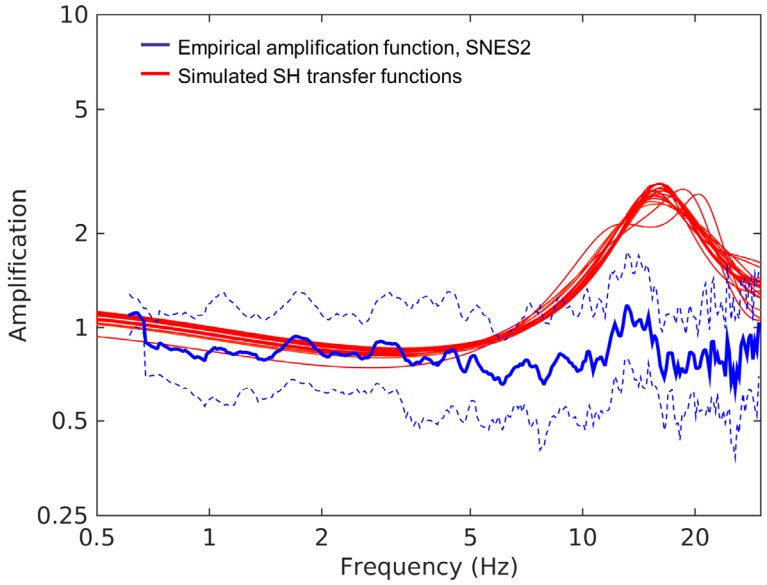

Figure 23 – Modeled SH transfer functions (black-to-yellow color scale) from the selected velocity profiles, corrected for the Swiss reference rock model, compared with the empirical amplification function from spectral modeling (blue line).

8 Conclusions

Active and passive seismic surveys were performed to characterize the structure of the subsurface below the SSMNet station SNES2. Active data were processed with the aim of deriving Rayleigh and Love wave dispersion curves, and of identifying the direct and refracted first-break arrivals of P-waves. Passive data were analyzed in a single-station fashion (H/V and polarization analysis), and

collectively (array) to estimate the Love and Rayleigh wave dispersion curve, and Rayleigh wave ellipticity.
The site is stiff with a shallow bedrock (about 10 m), therefore not particularly suitable for surface wave analysis. Besides, station SNES2 is located on top of an elongated ridge, where the assumption of 1D surface wave propagation does not hold true. As consequence, the performance of the passive array was poor, and the inversion process was mainly based on information from the active geophone line.
The velocity profile derived from the inversion process includes a thin (0.75 m thick) surficial layer with V_S = 167 m/s (soil cover); below, a layer with V_S = 641 m/s extends down to approximately 9.5 m depth. This is also the relative height of the ridge with respect to the surrounding area, so it is possible to argue that this material (probably moraine) forms the topographical feature where station SNES2 is located. Just below is the upper interface of the bedrock, having an S-wave velocity of about 1600 m/s, which should correspond to degraded limestone. V_S then increases gradually with depth, reaching approximately 2000 m/s at a depth of 30 m.
The fundamental frequency of the site, identified from H/V analysis of microtremor data to be around 2 Hz, corresponds therefore to a rock-to-rock interface at a depth much larger than that allowed by the acquired data (the latter being between 20 and 30 m). At higher frequency, circa 13 Hz, the empirical amplification function from spectral modeling of station SNES2 presents a peak which can be related to the resonance frequency of the ridge.
The obtained V_{S30} is 1021 m/s, thus classifying the soil as A type according to Eurocode 8 (CEN, 2004) and the SIA261 norm (SIA, 2014).

Acknowledgments

The authors thank Felicitas Stein and Dylan Longridge for their help during the measurements.

References

Arndt. L., 1932. La station séismologique de l'Observatoire astronomique et chronométrique de Neuchâtel. Bulletin de la Société Neuchâteloise des Sciences Naturelles, 57(1932), 187-198

Bergamo P., M. Hobiger, and D. Fäh, 2017. Site characterization report STSW2: Lac de Zeusier (VS) – Stausee.

Burjanek J,, G. Gassner-Stamm, V. Poggi, J.R. Moore and D. Fäh, 2010. Ambient vibration analysis of an unstable mountain slope. GJI, 180, 820-828.

CEN, 2004. Eurocode 8: Design of structures for earthquake resistance – Part 1: general rules, seismic actions and rules for buildings. European Committee for Standardization, en 1998-1 edition.

Edwards, B., Michel, C., Poggi, V., and Fäh, D. , 2013. Determination of Site Amplification from Regional Seismicity : Application to the Swiss National Seismic Networks. Seismological Research Letters, 84(4).

Fäh, D., F. Kind, and D. Giardini, 2001. A theoretical investigation of average H/V ratios. GJI, 145, no. 2, 535-549.

Foti, S., Lai C.G., Rix G.J., and C. Strobbia, 2015, Surface Wave Methods for Near-Surface Site Characterization: CRC Press, Taylor & Francis Group LLC.

Géli L, Bard P-Y, Jullien B (1988) The effect of topography on earthquake ground motion: a review and new results. Bull Seism Soc Am 78:42–63

Hobiger, M., P.-Y. bard, C. Cornou, and N. Le Bihan, 2009. Single station determination of Rayleigh wave ellipticity by using the random decrement technique (Raydec). GRL, 36, L14303

Joyner, W. B., Warrick, R. E., and Fumal, T. E., 1981. The effect of Quaternary alluvium on strong ground motion in the Coyote Lake, California, earthquake of 1979. Bulletin of the Seismological Society of America, 71(4):1333–1349.

Maranò, S., D. Fäh and Y. M. Lu, 2014. Sensor placement for the analysis of seismic surface waves: sources of error, design criterion and array design algorithms. GJI, 197, 1566-1581.

Maranò, S., 2016. http://mercalli.ethz.ch/~marra/WaveDec/userguide_WaveDec.html

Maranò, S., M. Hobiger, P. Bergamo and D. Fäh, 2017. Analysis of Rayleigh Waves with Circular Wavefront: a Maximum Likelihood Approach. GJI, 210 (3), 1570-1580.

Maraschini M., and S. Foti, 2010. A Monte Carlo multimodal inversion of surface waves. GJI, 182 (3). 1557 – 1566.

Michel, C., B. Edwards, V. Poggi., J. Burjanek, D. Roten, C. Cauzzi, and D. Faeh, 2014. Assessment of Site Effects in Alpine Regions through Systematic Site Characterization of Seismic Stations. BSSA, 104, no. 6, 2809-2826

Park, C. B., R. D. Miller, and J. Xia, 1999. Multichannel analysis of surface waves: Geophysics, **64**, 800–808.

Poggi, V., Edwards, B., and Fäh, D. (2011). Derivation of a Reference Shear-Wave Velocity Model from Empirical Site Amplification. Bulletin of the Seismological Society of America, 101(1):258–274.

Poggi, V., B. Edwards, and D Fäh, 2012. Characterizing the Vertical-to-Horizontal Ratio of Ground Motion at Soft-Sediment Sites. Bulletin of the Seismological Society of America, Vol. 102, No. 6, pp. 2741–2756

Poggi, V., and D. Fäh, 2010. Estimating Rayleigh wave particle motion from three component array analysis of ambient vibrations. GJI, 180, no. 1, 251-267.

Redpath, B. B., 1973, Seismic refraction exploration for engineering site investigations: National Technical Information Service, Technical Report E-73-4.

Reynolds, J.M., 2011, An introduction to applied and Environmental Geophysics: John Wiley & Sons, Ltd.

Roesset, J. (1970). Fundamentals of soil amplification. In Hansen, R. J., editor, Seismic Design for Nuclear Power Plants, pages 183–244. M.I.T. Press, Cambridge, Mass.

SIA, 2014. SIA 261 Einwirkungen auf Tragwerke. Société Suisse des ingénieurs at des architectes, Zurich, Switzerland.

Schmelzbach C., D. Sollberger, S. A. Greenhalgh, H. Horstmeyer, H. Maurer and J.O.A. Robertsson, 2016. 9C seismic data acquisition for near-surface applications: recording, wavefrom reciprocity and 4C rotation. 78th EAGE conference and exhibition. Extended abstract WS04 B03

Socco, L.V., and C. Strobbia, 2004, Surface-wave method for near-surface characterization: a tutorial: Near Surface Geophysics, 2, no. 4, 165-185.

Sollberger D., C. Schmelzbach, C. Van Renterghem, J. O. Robertsson and S. A- Greenhalgh, 2016. Single-component elastic wavefield separation at the free surface using source- and receiver-side gradients. SEG International Exposition and 86th annual meeting, 2268 – 2273.

Swisstopo, 2017. Atlas géologique de la Suisse, 1:25000, Feuille de Neuchâtel (CN1164).

Wathelet, M., 2008. An improved neighborhood algorithm: Parameter conditions and dynamic scaling. GRL, 35, no.9, 1-5.

Zeng C., J. Xia, R.D. Miller, G. P. Tsoflias, and Z. Wang, 2012. Numerical investigation of MASW applications in presence of surface topography. Journal of Applied Geophysics, 84, 52-60.